Electrical transport and Al doping efficiency in nanoscale ZnO films prepared by atomic layer deposition

Y. Wu' , P. M. Hermkens, B. W. H. van de Loo, H. C. M. Knoops, S. E. Potts, M. A. Verheijen, F. Roozeboom, and W. M. M. Kessels

Citation: Journal of Applied Physics **114**, 024308 (2013); doi: 10.1063/1.4813136
View online: http://dx.doi.org/10.1063/1.4813136
View Table of Contents: http://aip.scitation.org/toc/jap/114/2
Published by the American Institute of Physics

Electrical transport and Al doping efficiency in nanoscale ZnO films prepared by atomic layer deposition

Y. Wu,[1,2,a)] P. M. Hermkens,[1] B. W. H. van de Loo,[1] H. C. M. Knoops,[1] S. E. Potts,[1] M. A. Verheijen,[1] F. Roozeboom,[1,2] and W. M. M. Kessels[1]
[1]*Eindhoven University of Technology, PO Box 513, 5600 MB Eindhoven, The Netherlands*
[2]*Holst Centre, PO Box 8550, 5605 KN Eindhoven, The Netherlands*

(Received 15 April 2013; accepted 19 June 2013; published online 12 July 2013)

In this work, the structural, electrical, and optical properties as well as chemical bonding state of Al-doped ZnO films deposited by atomic layer deposition have been investigated to obtain insight into the doping and electrical transport mechanisms in the films. The range in doping levels from 0% to 16.4% Al was accomplished by tuning the ratio of ZnO and Al_2O_3 ALD cycles. With X-ray photoelectron spectroscopy depth profiling and transmission electron microscopy, we could distinguish the individual ZnO and AlO_x layers in the films. For films with a thickness of 40 nm, the resistivity improved from 9.8 mΩ cm for intrinsic ZnO to an optimum of 2.4 mΩ cm at 6.9 at. % Al. The binding energy of Zn $2p_{3/2}$ increased by 0.44 eV from the intrinsic ZnO to the highest Al-doped ZnO. This shift can be ascribed to an increase of the Fermi level. *Ex-situ* spectroscopic ellipsometry and Fourier transform infrared spectroscopy were used to measure the optical properties from which the carrier concentration and intra-grain mobility were extracted. The results showed that with increasing Al content, the grain boundary mobility increased at first due to an increased Fermi level, and then decreased mainly due to the scattering at AlO_x/ZnO interfaces. For the same reasons, the doping efficiency of Al for highly Al-doped ZnO dropped monotonically with increasing Al. Furthermore, a blue shift of the optical band-gap ΔE_g up to 0.48 eV was observed, consistent with the shifts of the Fermi level and the binding energy of the Zn $2p_{3/2}$ state. © *2013 AIP Publishing LLC*. [http://dx.doi.org/10.1063/1.4813136]

I. INTRODUCTION

ZnO is a transparent semiconductor with a wide and direct band gap of 3.4 eV. For this reason, ZnO-based thin films are widely studied (a) as semiconducting layers in thin-film transistors,[1] (b) as active layers in gas sensors,[2–6] and (c) as alternatives to indium tin oxide, which is currently used as a transparent conducting oxide (TCO)[7–10] in solar cells.[11] For the latter application, ZnO thin films doped with B,[12] Al,[13–15] Ga,[16] etc., have been actively investigated, due to their high conductivity, optical transparency, high thermal stability, and last but not least the high material abundance. Thin ZnO films (<100 nm) with relatively low resistivity (~1 mΩ cm) are generally desired for the aforementioned applications. For example, when used as a semiconducting layer in gas sensors, the sensitivity of ZnO maximizes[17] when the ZnO thickness is of the same scale of the Debye-length, which is in the order of 10 nm.[18]

Several deposition techniques have been reported for ZnO films, such as magnetron sputtering,[19] pulsed laser deposition,[20] chemical vapor deposition,[21] and atomic layer deposition (ALD).[22–25] Among these, ALD is considered to be a promising technique to deposit nanoscale ZnO films, because it is a self-limiting thin-film growth technique that guarantees excellent film conformality, uniformity, precise thickness control, sharp interfaces, as well as possibilities for creating reproducible and well-defined nanolaminate structures.[26] The doping concentration of doped ZnO can be precisely tuned by careful control of the ALD cycle ratio between the Zn and the dopant precursors. Therefore, the thickness, conductivity, and carrier density of the films can be controlled to meet stringent specifications.[27]

In the literature, Al-doped ZnO (AZO) films prepared by ALD have been investigated for their morphological, electrical, and structural properties as a function of Al concentration.[1,13,27–29] The chemical environment as well as the atomic charge of elements as a function of doping concentration still need to be studied in more detail, because the chemical bonding states of the elements (e.g., Al as an effective Al_{Zn}^{+} dopant in the ZnO lattice or Al within ineffective AlO_x clusters) determine the amount of free charge carriers in AZO thin films. The electrical properties regarding the charge transport, such as the Fermi level, charge carrier mobility within grains and at grain boundaries, are not fully understood either, while such parameters determine the performance of the AZO films as a semiconductor or transparent conductive oxide. Moreover, in order to understand how Al doping affects the crystallinity of ZnO films, the role of Al with respect to the structural and electrical properties of AZO films needs to be elucidated. The doping efficiency of Al should be calculated quantitatively for further characterization and comparison. All these parameters are important for a fundamental understanding of the doping mechanism, and consequently, the optoelectronic film properties of AZO as well.

Therefore, in this work, AZO films with various Al doping levels were prepared by ALD and characterized extensively.

a)Y.Wu@tue.nl

First, the thickness and deposition temperature were varied to find optimum values for the resistivity. Second, in order to figure out how the atomic distribution and crystallinity of AZO films affect their electrical properties, depth profiling X-ray photoelectron spectroscopy (XPS) and transmission electron microscopy (TEM) were used. Third, in order to obtain insight into the optical and electrical properties, spectroscopic ellipsometry (SE) and Fourier transform infrared spectroscopy (FTIR) were applied to derive the carrier density, intra-grain mobility, grain boundary mobility, and optical band gap. Next, the concept of Al doping efficiency was used to characterize the doping effect quantitatively. Finally, the shifts of the Fermi level were calculated and related to both the shifts of the binding energy and the optical band gap.

II. EXPERIMENTAL

A. Film preparation

Intrinsic ZnO (*i*-ZnO) and AZO films were deposited using an open-load Oxford Instruments OpAL^{TM} reactor. Si wafers with 450 nm thermally grown SiO_2 on top were used as substrates. Diethyl zinc [DEZ, $Zn(C_2H_5)_2$] and deionized water (DI H_2O) vapor were used as precursors for the deposition of *i*-ZnO films and the ZnO cycles in AZO films. The dosing and purging times in one ZnO cycle were DEZ (50 ms)/purge (5 s)/DI H_2O vapor (20 ms)/purge (6 s). Similarly, trimethyl-aluminium [TMA, $Al_2(CH_3)_6$] and DI H_2O vapor were used as precursors for the deposition of AlO_x layers in AZO films, with dosing and cycling times TMA (20 ms)/purge (3.5 s)/DI H_2O vapor (20 ms)/purge (3.5 s).

B. Electrical and structural analysis

The resistivity of the films was measured *ex-situ* at room temperature using a Signatone four-point probe (FPP), in combination with a Keithley 2400 Source Measurement Unit. Hall measurements were carried on a BioRad instrument. The XPS set-up used in this work was a Thermo Scientific K-Alpha KA1066 spectrometer using monochromatic Al Kα X-ray radiation ($h\nu = 1486.6$ eV). Photoelectrons were collected at a take-off angle of 60°, as measured from the surface normal. A 400-μm diameter X-ray spot was used in the analyses. A flood gun was used to correct for possible sample charging. Furthermore, all samples were corrected for sample charging using the Si 2p orbital from the Si substrate as an internal reference with a binding energy of 99.3 eV.[30] For XPS depth-profiling, an Ar-gun with a voltage of 1000 eV and high current (17.9 μA) was applied to sputter the *i*-ZnO and AZO films. The sputtering rate in this setting was ~0.13 nm/s. Cross-sectional TEM studies on FIB lift-out samples were performed in bright field and in high-angle annular dark-field (HAADF) modes using a FEI Tecnai F30ST transmission electron microscope (TEM).

C. Optical analysis

The SE measurements were performed using a J.A.Woollam Co. Inc. M-2000D spectrometer with an XLS-100 light source (1.2–6.5 eV of photon energy).[31] A Psemi-M0 model[32] was applied in the data analysis to extract information on the material properties, such as the thickness, and on the optical parameters, in particular on the dielectric constants ε_1 and ε_2. Furthermore, the reflectance was measured by using a Bruker Tensor 27 reflectance-FTIR instrument in the photon energy range of 0.12–0.86 eV. A Drude oscillator model[33,34] was used afterwards to extract the optical mobility and carrier density from the combined data obtained from reflectance-FTIR and the SE. Details of the modeling will be described in a separate publication.[35]

III. RESULTS AND DISCUSSION

A. Intrinsic ZnO

For *i*-ZnO films, the effects of film thickness and growth temperature on their resistivity were studied, as shown in Fig. 1. Figure 1(a) shows the resistivity of *i*-ZnO films as a function of thickness. In order to avoid possible issues with the aging effect of ZnO films, the resistivity and the thickness were measured directly after the deposition (within 30 min) by FPP and SE, respectively. Based on the curve in Fig. 1(a), a critical thickness (D_0) and the corresponding resistivity (ρ_0) can be defined as $D_0 = 40$ nm and $\rho_0 = 11.0$ mΩ cm, respectively. For films with thicknesses above D_0, the resistivity does not improve significantly, while below D_0, the resistivity increases significantly as the thickness decreased. According to Kasap's model on polycrystalline thin films,[36] the scattering of electrons at the surface, interface, and grain boundaries during the electrical transport may lead to such a phenomenon. The mean free path of electrons is limited when the thickness of the film is below its critical value D_0. Meanwhile, a lower degree of crystallinity and smaller grain size in the initial layer might also limit the electrical properties. Therefore, a thickness of ~40 nm was chosen as a

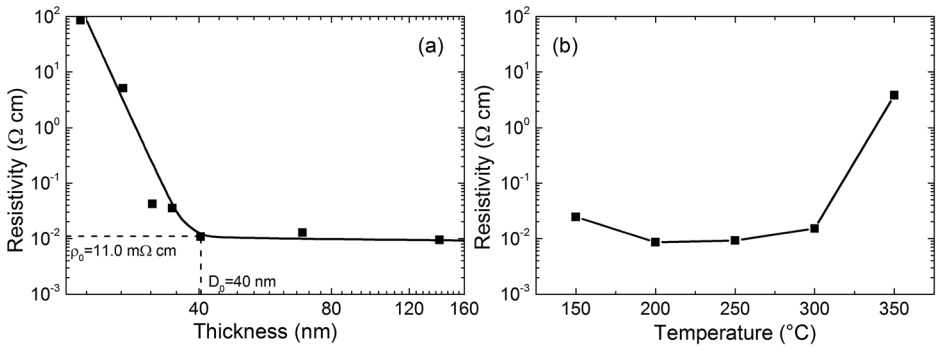

FIG. 1. (a) Resistivity of *i*-ZnO films grown on 450 nm SiO_2/*p*-Si substrates at 300 °C as a function of film thickness. The critical thickness (D_0) and the corresponding resistivity (ρ_0) are indicated in the figure. When the thickness of *i*-ZnO films is below the critical value, the resistivity increases abruptly. (b) Resistivity of 40 nm *i*-ZnO films deposited on 450 nm SiO_2/*p*-Si substrate as a function of the substrate temperature.

standard for further investigation of AZO film growth. As mentioned in the Introduction, ZnO films with thickness well below 100 nm and with a relatively low resistivity are desired to meet the requirements of various applications.

The effect of the growth temperature on the resistivity of *i*-ZnO is shown in Fig. 1(b). The optimum growth temperature with respect to minimum resistivity was between 200 °C and 250 °C. Similar results have been described in other reports where the lower resistivity at the temperature between 200 °C and 250 °C was ascribed to a higher carrier density[37–40] of *i*-ZnO films, compared to other growth temperatures. Furthermore, the same *i*-ZnO films were deposited on glass substrate for comparison. The result showed that the resistivity of the films on glass substrates was slightly higher than that of films grown on thermal oxide 450 nm SiO_2/*p*-Si substrate. Based on the aforementioned results, a thickness of 40 nm, growth temperature of 250 °C, and substrates of thermal oxide 450 nm SiO_2/*p*-Si were chosen for our study on AZO films.

B. Al-doped ZnO

A series of AZO films was prepared with different aluminum concentrations. The aluminum concentration was denoted as "aluminum fraction" (*AF*), and defined as the atomic ratio Al/(Al + Zn) that is the fraction of Zn atoms replaced with Al. In order to prepare a particular AZO film with a certain *AF*, one TMA cycle was inserted after a certain number *m* of DEZ cycles. Thus, one "supercycle" of AZO film was defined as *m* cycles of DEZ plus one subsequent TMA cycle, and *m* is called "cycle ratio." The total number of supercycles *M* and the cycle ratio *m* were chosen to target a nominal thickness of around 40 nm for each sample on the basis of the growth per cycle (GPC) for pure ZnO and Al_2O_3

$$Thickness = M \times (GPC_{ZnO} \times m + GPC_{Al_2O_3}). \quad (1)$$

Typical GPC values of pure ZnO films at 250 °C were 0.16 nm/cycle. The GPC of a single Al_2O_3 cycle on a ZnO matrix is 0.15 nm/cycle, as determined using *in-situ* SE. The nominal Al fraction AF_{Nom} was calculated based on the GPCs by

$$AF_{Nom} = \frac{GPC_{Al_2O_3}}{GPC_{Al_2O_3} + GPC_{ZnO} \times n} \times 100\%. \quad (2)$$

Depth-profiling XPS was used to measure the atomic percentage of Al, Zn, C, and O throughout the films (indicated by $Al_{at.}\%$, $Zn_{at.}\%$, etc.), and, consequently, the actual Al fraction AF_{XPS} was calculated by

$$AF_{XPS} = \frac{Al_{at.}\%}{Al_{at.}\% + Zn_{at.}\%} \times 100\%. \quad (3)$$

The interspacing *l* between adjacent AlO_x layers was determined by $l = D/M$, where *D* is the total thickness of the AZO films.

In total, 11 AZO samples were prepared with varying *AF* values. The parameters are listed in Table I. The nominal *AF* (AF_{Nom}) was found to deviate from the AF_{XPS}, especially at high AF_{Nom} values, as presented in Fig. 2(a). The nucleation delay of ZnO on an AlO_x matrix[41] has been reported to be the reason for such a deviation: the actual GPC_{ZnO} after one Al_2O_3 cycle was smaller than that on bulk ZnO matrix. Therefore, in our further analysis and discussion, the doping level of aluminum is described in terms of AF_{XPS}, instead of AF_{Nom}.

The atomic percentages of Zn, Al, and O with different AF_{XPS} are presented in Fig. 2(b). First, no carbon was detected throughout the films. Carbon was only present as surface contamination. Second, the atomic percentage of O increased at higher AF_{XPS}. In the ideal case, if all of the aluminum atoms would be incorporated as dopants substituting the Zn atoms in the form of Al_{Zn}^{+}, the aluminum doping would not lead to additional oxygen atoms in the AZO films. Thus, the increase of oxygen content suggests the existence of an Al_2O_3-like phase in the AZO films, since the O atomic percentage is larger in Al_2O_3 than in a pure ZnO.

Figure 3(a) shows the distribution of Al, Zn, O, and Si elements of an AZO film along the growth direction as obtained by depth-profiling XPS. The sample corresponding to Fig. 3(a) was deposited with the same recipe as sample 03 in Table I, but on a *p*-Si substrate with ~1.5 nm native SiO_2 instead of 450 nm thermally grown SiO_2. This ~40 nm AZO

TABLE I. Properties of AZO films deposited by thermal ALD at 250 °C on *p*-Si substrates with 450 nm thermal oxide SiO_2. AF_{Nom} is the nominal aluminum fraction defined by Eq. (2). The actual aluminum fraction was calculated from Eq. (3) using the atomic percentage obtained from depth-profiling XPS, and is denoted as AF_{XPS}. Thicknesses were determined from SE data, which were analyzed using the Psemi-M0 model.[32] The error in the thickness values is typically <1 nm.

Sample ID	Cycle Ratio *m*	Supercycle *M*	AF_{Nom} (%)	AF_{XPS} (%)	Thickness *D* (nm)	Interspacing of AlO_x *l* (nm)
01	N/A	N/A	0	0	41.2	N/A
02	126	2	0.7	0.9	40.7	20.4
03	85	3	1.1	1.9	41.1	13.7
04	51	5	1.8	3.0	40.1	8.0
05	36	7	2.5	4.1	40.4	5.8
06	28	9	3.2	5.9	38.9	4.3
07	23	11	3.9	6.9	41.4	3.8
08	18	13	5.0	9.4	39.6	3.0
09	16	15	5.5	11.0	40.1	2.7
10	14	17	6.3	13.1	39.7	2.3
11	12	19	7.2	16.4	38.2	2.0

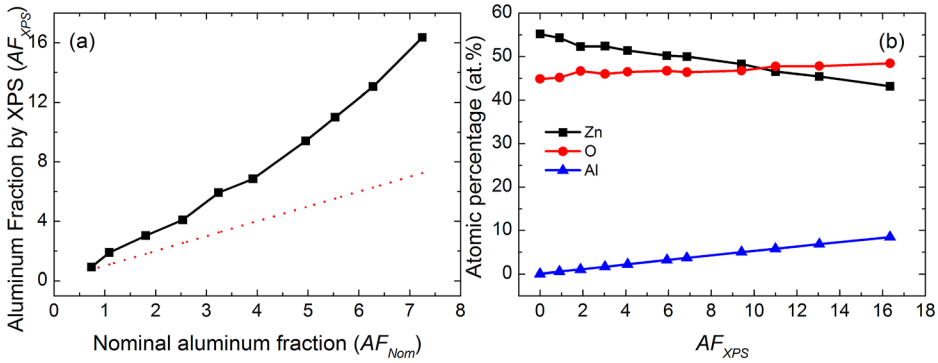

FIG. 2. (a) Aluminum fraction measured by XPS as a function of nominal aluminum fraction in the AZO films. The relation for the nominal aluminum fraction is indicated by the dotted line. (b) Atomic percentage of Zn, O, and Al measured by XPS for various aluminum fractions AF_{XPS}.

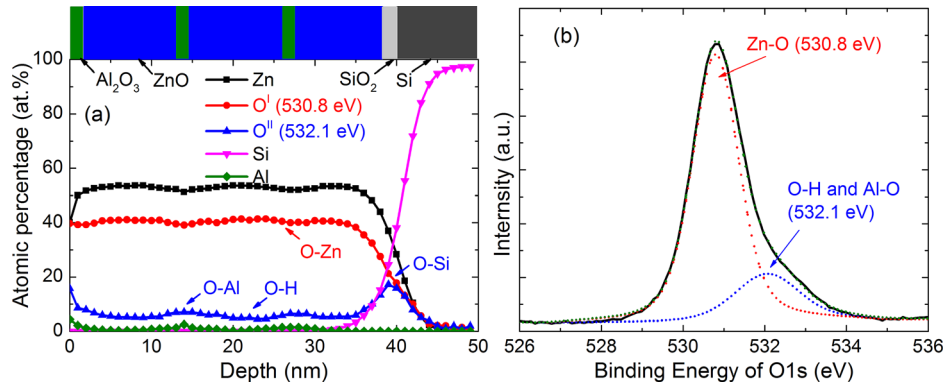

FIG. 3. (a) Atomic percentage of Zn, O, Al, and Si elements as a function of depth from the surface as determined by depth-profiling XPS. The schematic representation above the graph shows the structure of the AZO film. The ALD recipe used for this sample was similar to the one for sample 03 listed in Table I, but here a ~1.5 nm native SiO_2/*p*-Si was used as a substrate instead of 450 nm thermal oxide SiO_2/*p*-Si. (b) XPS spectrum of O 1s peak for sample 03 at a depth of 14 nm. The oxygen peak was deconvoluted into two components with different binding energies. The component of 532.1 eV can be attributed to both O-Al and O-H bonds. The component at 530.8 eV can be attributed to Zn-O bonds.

film deposited from 3 supercycles contains basically three separate AlO_x/ZnO stacks. At around 40 nm depth, the Zn and O levels dropped to zero, and Si appeared, reaching 100 at. % at the interface between the AZO film and the Si substrate. In the XPS depth profile, Al signals appear at certain depths, consistent with the schematic representation of the sample in the graph. Such a periodic variation in atomic percentage suggests the presence of a nanolaminate structure, resulting from the ALD deposition scheme.[42,43] The nanolaminate structure was confirmed by TEM imaging as well, as shown in Fig. 4(a). Figure 4(a) shows a HAADF STEM image of sample 03. The contrast in the imaging mode is caused by the mass difference between the elements. Within the bulk of the film, the image reveals two AlO_x layers with a lower atomic number, i.e., layers with a higher Al content. The high resolution TEM image of Fig. 4(b) gives more information about the morphology of the AZO films. AZO grains appear separated into three regions and two AlO_x layers are located at the interfaces between these regions. The image shows clearly that Al_2O_3 ALD cycles have interrupted the growth of the ZnO grains and that new ZnO grains nucleated after the individual Al_2O_3 ALD cycles. The latter is also in agreement with X-ray diffraction patterns of the AZO films, which revealed that the crystallinity of the films decreases at higher *AF*, as reported in the literature.[13,41]

The nanolaminate structure was observed in the AZO films with low AF_{XPS} (samples 01–06), while for the AZO films with higher AF_{XPS} (samples 07–11), the atomic distribution of Al, Zn, and O could no longer be resolved with XPS. The resolution of XPS in the growth direction is limited to $l_r \approx 5$–10 nm, so when the interspacing between adjacent AlO_x layers l is less than l_r ($l < l_r$), the discrete nanolaminate structure can no longer be resolved by XPS.

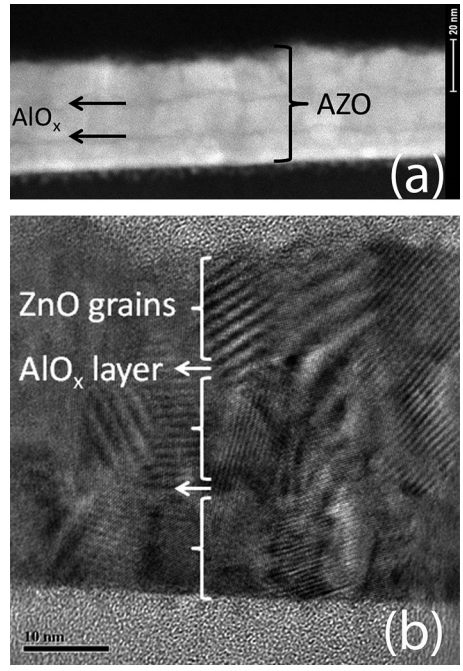

FIG. 4. Cross-sectional HAADF (a) and high-resolution TEM (b) images of sample 03. The ALD recipe existed of 3 supercycles of AlO_x/ZnO. The AZO film was ~40 nm thick (see Table I).

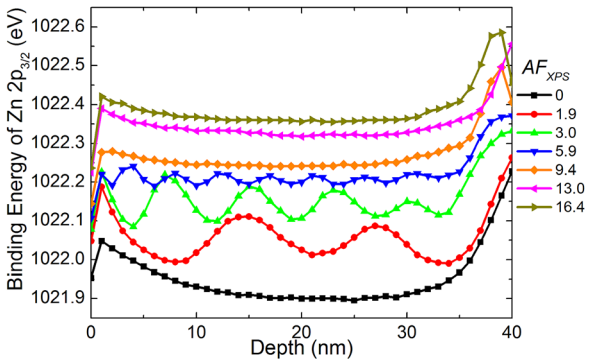

FIG. 5. XPS depth profiles for the Zn $2p_{3/2}$ signal of several AZO samples.

The O peak in Fig. 3(b) contains contributions of two components with different binding energies. The lower binding energy component of the O 1s peak at 530.8 eV can be attributed to O^{2-} ions surrounded by Zn^{2+} ions, indicating the Zn-O bonds[25,44–48] and is denoted by O^{I} in Fig. 3(a). This O signal intensity shows the same variation as the Zn signal intensity, which confirms the chemical bonding state of O^{2-} co-ordinated with Zn^{2+}. The second O component at the binding energy of 532.1 eV denoted by O^{II} in Fig. 3(a) can be assigned mainly to hydroxyl groups (−OH),[25,44–48] which spread throughout the AZO film. However, in Fig. 3(a), the O^{II} component shows the same variation with the Al content, meaning that part of this O^{II} component at binding energy of 532.1 eV can be attributed to O^{2-} ions coupled with Al^{3+}. Such O-coupled Al^{3+} might be present as Al_{Zn}^{+} in the ZnO phase, but also as AlO_x clusters. In theory, it should be possible to distinguish these two Al^{3+} environments by the Al 2p peak fitting. Yet, in practice, the low Al doping level resulted in intensities too low for the Al 2p peak to investigate the chemical environment. The atomic percentage of the O^{II} component reached a maximum at the interface. This part of the O^{II} component was assigned to O in the ~1.5 nm thick native SiO_2.

The binding energy of Zn $2p_{3/2}$ in AZO films with various AF_{XPS} throughout the films was measured by depth-profiling XPS and is presented in Fig. 5. The binding energy at the surface (depth = 0 nm) deviated due to the surface contamination. The higher binding energy at the interface (depth = 35–40 nm) can be ascribed the different chemical bonding state of Zn on the SiO_2 matrix. Excluding these two effects, the binding energies generally shifted to higher values with higher AF_{XPS}. This shift was observed consistently for both the bulk of the AZO films (0 nm < depth < 40 nm) and for the surfaces (depth = 0 nm). Therefore, a possible sputtering effect during sample examination cannot be the reason for such a shift. Since the binding energies are referenced to the Fermi level (E_F),[30,49,50] the increase can be attributed to an increase in E_F.[51,52] That is, the Al doping contributes free electrons to the AZO films, leading to a higher E_F. Furthermore, for the samples with low AF_{XPS}, the binding energy of Zn $2p_{3/2}$ oscillates throughout the films, with an amplitude of around 0.1 eV. Again, taking sample 03 as an example ($AF_{XPS} = 1.9\%$), it is clear that the binding energy reaches its local maximum where the AlO_x layers are located. A possible mechanism that can be proposed to explain the oscillation is the following. The Al_{Zn}^{+} in the ZnO lattice can serve as an effective positive charge and create a local static electric field.[42] The electric field can affect the surrounding atoms. Core electrons from adjacent Zn atoms may shift towards the Al_{Zn}^{+} centre by the electrostatic force, leading a higher atomic charge of the Zn. It was found that a higher atomic charge can cause a higher binding energy in the measurement of XPS.[53–55] Therefore, the local maxima can be ascribed to the delocalization of core electrons of Zn towards Al_{Zn}^{+}. For samples with high AF_{XPS}, such oscillations can no longer be observed since the interspacing between the adjacent AlO_x layers is within the depth resolution of XPS. In summary, the increase of the free electron density can cause a shift in the binding energy globally which manifests as an increase in E_F. Meanwhile, according to the mechanism proposed by us, the delocalization of Zn core electrons by Al_{Zn}^{+} centres leads to a local increase of the binding energy.

The carrier density and optical mobility are presented in Fig. 6(a). The carrier densities from Hall measurements and the optical modeling (using SE and FTIR data) are consistent with each other, which confirms the accuracy of our modeling and validates the value of the electron effective mass ($m^* = 0.4\,m_e$) that we used here. The average distance an electron travels while interacting with a photon is much shorter than the average grain size. Hence, it can be assumed that for optical measurements, the grain boundary scattering can be neglected. Therefore, the mobility derived from modeling SE and FTIR measurements μ_{opt} can be assumed to be equal to the intra-grain mobility as $\mu_{opt} \approx \mu_{intra\text{-}grain}$.[56] The intra-grain mobility is considered to be determined by

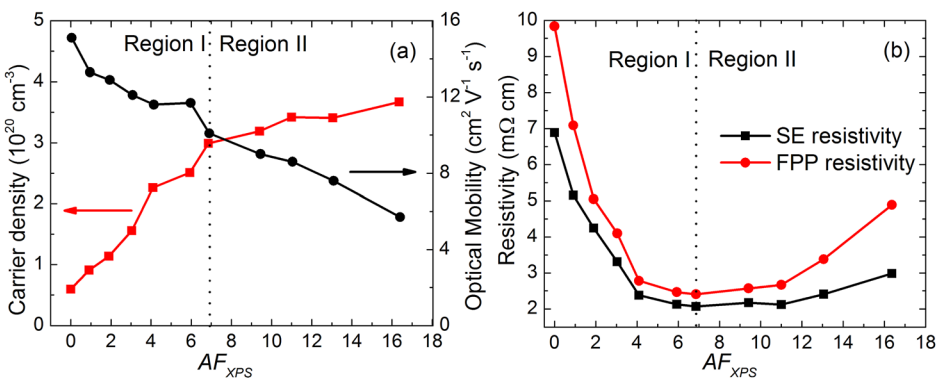

FIG. 6. (a) Carrier density and optical mobility as a function of AF_{XPS}, as extracted from SE and FTIR data. (b) Intra-grain resistivity (SE resistivity) and effective resistivity (FPP resistivity) as a function of AF_{XPS}.

ionized and neutral impurity scattering, etc.[57] The intra-grain resistivity can be defined as

$$\rho_{intra-grain} = (e \times n \times \mu_{opt})^{-1}, \quad (4)$$

where e, n, and μ_{opt} are the elementary charge, carrier density, and optical mobility, respectively. Both the optically determined intra-grain resistivity and the electrically determined effective resistivity (measured by FPP) are plotted in Fig. 6(b). The difference between both curves was ascribed to scattering at grain boundaries. In the FPP series of the effective resistivity, the resistivity was improved from 9.8 mΩ cm for intrinsic ZnO to an optimum of 2.2 mΩ cm at $AF_{XPS} = 6.9\%$. The optically determined intra-grain resistivity also shows an optimum value at the same value of AF_{XPS}. Thus, the AZO series can be classified into two regions: region I with samples 01–06, and region II with samples 08–11, and with sample 07 just on the borderline, as denoted in Figs. 6(a) and 6(b). In Fig. 6(a), the carrier density increases significantly with the addition of Al doping in region I, since Al species in the form of Al_{Zn}^{+} in the ZnO lattice release electrons and contribute a number of free electron carriers to the AZO films. However, in region II, the increase of the carrier density shows a soft saturation. This behavior can be explained by Lee's model.[42] as shown in Fig. 7. Since Al-doping mainly occurs at the interface of the ZnO and AlO_x layers, Al_{Zn}^{+} creates an effective electric field at the position of the AlO_x layers. At high values of AF_{XPS}, more AlO_x layers are deposited within the 40 nm AZO films such that the interspacing of adjacent AlO_x layers becomes smaller. When the interspacing is larger than a critical value ($l > l_c$), as shown in Fig. 7(a), the effective electric fields from adjacent AlO_x layers do not overlap each other, and Al doping is relatively efficient. Therefore, the carrier density shows a significant increase with higher Al doping at region I. When $l < l_c$, as shown in Fig. 7(c), the effective electric fields overlap each other. According to Lee's model, this overlap can inhibit further Al-doping by the repulsion between adjacent electrons or charged donors.[42] Therefore, in region II, the addition of Al atoms no longer contributes to the carrier density effectively. On the basis of the different trends of carrier density between regions I and II, the critical interspacing can be defined as the value of sample 07 ($l_c = 3.8$ nm), as shown in Fig. 7(b). Moreover, the optical mobility decreases gradually with additional doping in the entire Al-doping range, as shown in Fig. 6(a). As discussed before, effective Al_{Zn}^{+} dopants act as ionized impurities, while the rest of the Al atoms in ZnO lattice form neutral impurities.[58] Both types of Al species are point defects and will lead to the scattering of free carriers during the electrical transport within ZnO grains.[57]

Next, in order to study the role of the Al species at the grain boundaries, the effective mobility and the grain boundary mobility can be calculated from Matthiessen's rule by

$$\rho_{eff} = (e \times n \times \mu_{eff})^{-1}, \quad (5)$$

$$\mu_{eff}^{-1} = \mu_{intra-grain}^{-1} + \mu_{GB}^{-1}, \quad (6)$$

where ρ_{eff} is the effective resistivity measured by FPP, e is the elementary charge, n is the carrier density derived from optical analysis, and μ_{eff}, $\mu_{intra-grain}$, and μ_{GB} are the effective, intra-grain mobility and grain boundary mobility, respectively. As plotted in Fig. 8(a), with increasing AF_{XPS}, μ_{GB} increases slightly in region I while decreasing strongly in region II. Such a phenomenon can be explained according to the band diagram at grain boundaries, as presented in Fig. 8(b).[57] In AZO films, defects at grain boundaries are charged by

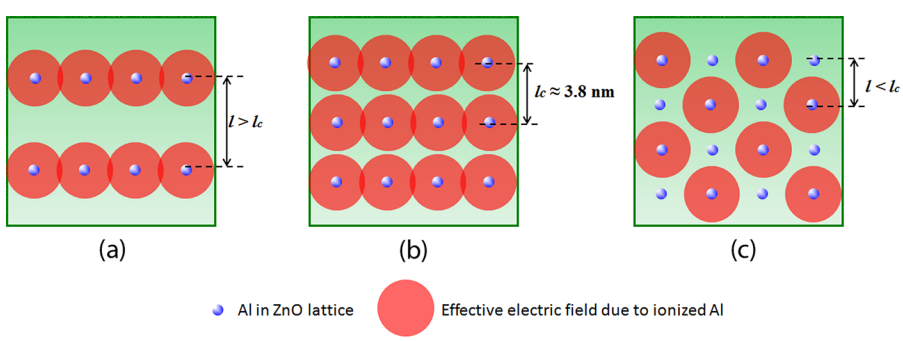

FIG. 7. Schematic representations of the effective electric field of Al_{Zn}^{+} in the ZnO lattice: (a) in region I, Al_{Zn}^{+} donates electrons effectively when $l > l_c$; (b) transition region between regions I and II, $l_c \approx 3.8$ nm, corresponding to sample 07; (c) in region II, the effective electric field prohibits further doping when $l < l_c$. l_c is the critical interspacing between AlO_x layers in the film's growth direction. (After Lee *et al.*, Ref. 42).

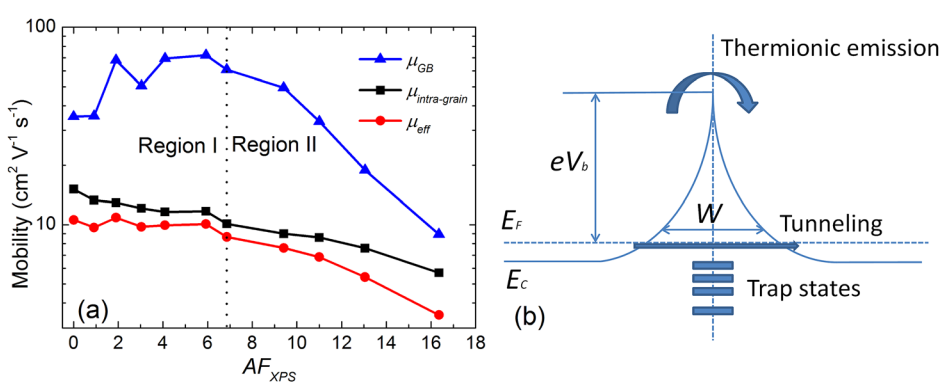

FIG. 8. (a) Effective mobility μ_{eff}, intra-grain mobility $\mu_{intra-grain}$, and grain boundary mobility, μ_{GB}, as a function of the aluminum fraction AF_{XPS}, (b) Schematic representation of the energy diagram at grain boundaries. (eV_b: barrier height; W: barrier width; E_F: Fermi level; and E_C: energy level of the conduction band tail.)

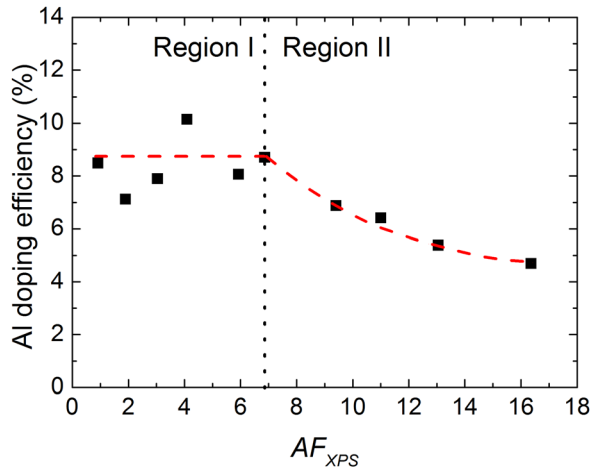

FIG. 9. Al doping efficiency as a function of aluminum fraction (AF_{XPS}). The dashed curve is a guide to the eye.

electrons, leading to trapping states and barriers at grain boundaries. The electron transport through grain boundaries can then be described by the classical thermionic emission and quantum-mechanical tunneling.[57] In region I, the increased carrier density will lead to a shift of the Fermi level to a higher energy level. Therefore, the effective barrier height and width become smaller, and consequently, the grain boundary mobility will increase at higher AF_{XPS}. In region II, the interspacing between the adjacent AlO_x layers becomes smaller than the critical value ($l < l_c$), and the scattering at the interface of the ZnO layers and AlO_x layers becomes dominant. Such a scattering limits the mean free path of free electrons during the electrical transport. Meanwhile, as discussed before, AlO_x interrupts the nucleation and growth of ZnO grains during deposition. At high AF_{XPS}, the closely spaced AlO_x layers result in smaller ZnO grain sizes, and more grain boundaries between ZnO gains. As a result, the grain boundary mobility decreases significantly at higher AF_{XPS} in region II.

The Al doping efficiency η of Al is the fraction of Al atoms, which contribute to the carrier density by the following mechanism:

$$Al_{Zn} \rightarrow Al_{Zn}^{+} + e^{-}.$$

The doping efficiency can be calculated by the following equation:

$$\eta = \frac{n - n_0}{N_{Zn} \times AF_{XPS}} \times 100\%. \quad (7)$$

In Eq. (7), n and n_0 are the carrier density of AZO and intrinsic ZnO, respectively. AF_{XPS} is the aluminum fraction as measured by XPS, and N_{Zn} is the atomic density of Zn. Therefore, the product of N_{Zn} and AF_{XPS} yields the atomic density of Al. By Rutherford backscattering spectrometry (RBS), N_{Zn} for intrinsic ZnO was measured to be $4.0 \times 10^{22}\,cm^{-3}$. The physical meaning of the doping efficiency is the percentage of Al atoms, which effectively donate free electrons to the AZO films. The calculated result is plotted in Fig. 9. As can be seen, η is less than 10% for the entire AZO series. As estimated by RBS, the average distance between adjacent Al atoms within the same AlO_x layer was around 0.5–1 nm. As illustrated in Fig. 7(a), the overlapping of the effective electric field in the same AlO_x layer inhibits the release of free electrons. Therefore, the number of effective Al donors was limited ($\eta < 10\%$). Moreover, in region I, η was relatively constant, varying from 7% to 10%, implying that the effective electric field from AlO_x layers in the growth direction does not inhibit the release of free electrons from Al_{Zn}^{+} when the interspacing l is large enough. In region II, as explained before, η decreases monotonically with increasing AF_{XPS} due to the overlapping effective electric field from the AlO_x layers.

As is common for AZO thin films, the optical band gaps of the films were derived from the so-called Tauc plots, as depicted in Fig. 10(a), which shows $(\varepsilon_2 E^2)^2$ as a function of photon energy for the AZO film series. ε_2 is the imaginary part of the dielectric function $\varepsilon_2(\omega)$, which was extracted from the SE data in the range of 1.2−6.5 eV. E is the photon energy. Since ZnO has a direct band-gap, the optical band gap or Tauc gap (E_g) is defined as the photon energy, where the extrapolation of the linear part of $(\varepsilon_2 E^2)^2$ vs. E intersects the horizontal axis.[59] The resulting E_g values for each AF_{XPS}

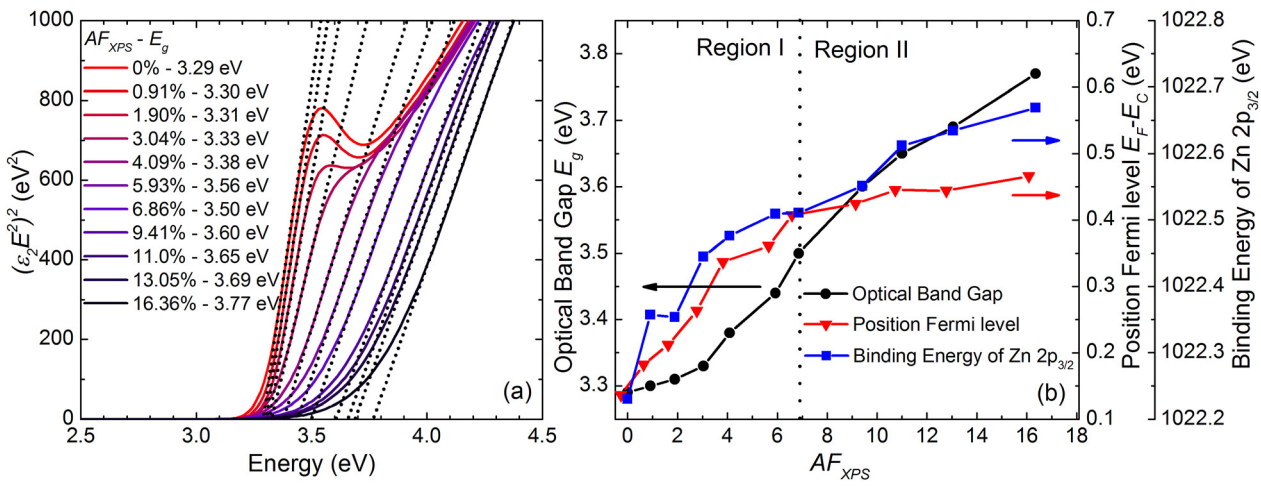

FIG. 10. (a) Tauc plots of $(\varepsilon_2 E_2)^2$ vs. photon energy for AZO films with different aluminum fractions (AF_{XPS}) to extract the optical band gap values (E_g); (b) Comparison of the shifts of optical band gap (E_g), the Fermi level (E_F-E_C), binding energy of Zn 2p$_{3/2}$ as a function of AF_{XPS}. Note that the absolute values of these three parameters are different while the scale intervals are equal (0.1 eV per division).

are listed in the legend of Fig. 10(a). Note that the value of ε_2 can also be affected by exciton absorption in ZnO,[60] which might slightly affect the resulting E_g values.

The increase of E_g for higher AF_{XPS} values as observed in Fig. 10(a) is mainly due to the shift of the Fermi level, according to the Burstein-Moss effect.[61] For a more detailed comparison, the shift of the Fermi level was evaluated on the basis of the carrier density. Given that *i*-ZnO and AZO are degenerate semiconductors, the following equations apply:

$$n = \int_{E_c}^{\infty} D_C(E) f(E,T) dE, \tag{8}$$

$$D_C(E) = \frac{(2m^*)^{3/2}}{2\pi^2\hbar^3}\sqrt{E - E_C}, \tag{9}$$

$$f(E,T) \approx \frac{1}{\exp[(E - E_F)/k_B T] + 1}, \tag{10}$$

where n is the electron density, and $D_C(E)$ and $f(E,T)$ stand for the density of states in the conduction band and the Fermi distribution function at an energy E, respectively. T is the temperature (300 K in the present case), E_c is the energy level of the conduction band tail, m^* is the effective electron mass, which is assumed to be $0.40\,m_e$, and $\hbar$ and k_B are the Dirac constant and Boltzmann constant, respectively. From Eqs. (8) to (10), the relationship between the carrier density and the height of the Fermi level can be obtained. Hence, the position of the Fermi level related to the conduction band tail (E_F-E_c) can be calculated as a function of the carrier density. The resulting plot is presented in Fig. 10(b).

The optical band gap (E_g), and the Fermi level (E_F-E_C), and the binding energy of Zn $2p_{3/2}$ (averaged over the film thickness, see in Fig. 5) are compared in Fig. 10(b). All three curves show a monotonic increase with increasing AF_{XPS}. As explained before, the shifts of E_g and the binding energy were both attributed to the increase of the Fermi level. Consequently, in principle, all of these three parameters should shift with the same trend and within the same order of magnitude with the carrier density. As presented in Fig. 10(b), the difference between *i*-ZnO and the highest doped ZnO ($AF_{XPS} = 13.6\%$) was 0.48 eV for E_g, 0.33 eV for E_F, and 0.44 eV for the binding energy. This supports therefore the explanation that the shift of E_F with carrier density is the main reason for the increase of E_g and the binding energy. However, the shift of E_g ($\Delta E_g = 0.48$ eV) is larger than that of E_F ($\Delta E_F = 0.33$ eV). The difference can be qualitatively explained by the existence of the AlO_x layers within the ZnO. Since amorphous Al_2O_3 films have a larger E_g ($E_g = 6$–7 eV (Ref. 62)) than ZnO, the AlO_x layers in the AZO films might cause an additional increase of the E_g of the entire film. The binding energy also has a larger shift ($\Delta BE = 0.44$ eV) than E_F. As discussed before, the delocalization of the core electrons from Zn may contribute a higher binding energy of Zn $2p_{3/2}$, in the order of 0.1 eV.

IV. CONCLUSION

In this work, we have studied the structural, electrical, and optical properties of AZO films with various doping levels as deposited by ALD. The resistivity of the films improved from 9.6 mΩ cm for intrinsic ZnO to an optimum of 2.4 mΩ cm for Al-doped ZnO with an Al fraction of 6.9%. By depth-profiling XPS, a nanolaminate structure of AlO_x/ZnO layers could be resolved for Al doping levels up to 5.9%. A nanolaminate structure was also observed by cross-sectional TEM. The AlO_x layers cause interface scattering during the electrical transport in ZnO layers. This effect is the main reason for the reduced mobility at grain boundaries at high doping level. At high doping levels, the carrier density also shows a soft saturation. We postulate that the effective electric field generated by Al_{Zn}^{+} centres limits the doping efficiency when the interspacing of the adjacent AlO_x layers becomes smaller at higher doping levels. A blue shift of the optical band-gap ($\Delta E_g = 0.48$ eV) was observed, and shown to be consistent with the shifts of both the Fermi level and the binding energy of Zn $2p_{3/2}$ photoelectrons.

ACKNOWLEDGMENTS

The authors thank Dr. M. Blauw (Holst Centre) for his help in the Hall measurements. W. Keuning and Dr. T. Fernández Landaluce are acknowledged for doing the XPS measurements and related analysis. S. Smit is thanked for his contribution to the theoretical calculation of the Fermi level. The financial support by IMEC-NL within the Holst Centre in Eindhoven, The Netherlands, is gratefully acknowledged.

[1]W. J. Maeng, S.-J. Kim, J.-S. Park, K.-B. Chung, and H. Kim, J. Vac. Sci. Technol. B **30**, 031210 (2012).
[2]M. Kudo, T. Kosaka, Y. Takahashi, H. Kokusen, N. Sotani, and S. Hasegawa, Sens. Actuators B **69**, 10 (2000).
[3]D. Barreca, D. Bekermann, E. Comini, A. Devi, R. A. Fischer, A. Gasparotto, C. Maccato, G. Sberveglieri, and E. Tondello, Sens. Actuators B **149**, 1 (2010).
[4]J. Müller and S. Weissenrieder, Fresenius' J. Anal. Chem. **349**, 380 (1994).
[5]S.-J. Chang, T.-J. Hsueh, I.-C. Chen, and B.-R. Huang, Nanotechnology **19**, 175502 (2008).
[6]S. O'Brien, M. G. Nolan, M. Çopuroglu, J. A. Hamilton, I. Povey, L. Pereira, R. Martins, E. Fortunato, and M. Pemble, Thin Solid Films **518**, 4515 (2010).
[7]A. E. Delahoy and S. Guo, *Handbook of Photovoltaic Science and Engineering*, 2nd ed. (John Wiley & Sons, Ltd, New York, 2011), pp. 716–796.
[8]F. Ruske, M. Roczen, K. Lee, M. Wimmer, S. Gall, J. Hüpkes, D. Hrunski, and B. Rech, J. Appl. Phys. **107**, 013708 (2010).
[9]E. Fortunato, D. Ginley, H. Hosono, and D. C. Paine, MRS Bull. **32**, 242 (2007).
[10]J. N. Duenow, T. A. Gessert, D. M. Wood, T. M. Barnes, M. Young, B. To, and T. J. Coutts, J. Vac. Sci. Technol. A **25**, 955 (2007).
[11]J. a van Delft, D. Garcia-Alonso, and W. M. M. Kessels, Semicond. Sci. Technol. **27**, 074002 (2012).
[12]A. Favier, D. Muñoz, S. Martín de Nicolás, and P.-J. Ribeyron, Sol. Energy Mater. Sol. Cells **95**, 1057 (2011).
[13]P. Banerjee, W.-J. Lee, K.-R. Bae, S. B. Lee, and G. W. Rubloff, J. Appl. Phys. **108**, 043504 (2010).
[14]J. Y. Kim, Y.-J. Choi, H.-H. Park, S. Golledge, and D. C. Johnson, J. Vac. Sci. Technol. A **28**, 1111 (2010).
[15]J. Elam and S. George, Chem. Mater. **15**, 1020 (2003).
[16]K. T. R. Reddy, T. B. S. Reddy, I. Forbes, and R. W. Miles, Surf. Coat. Technol. **151–152**, 110 (2002).
[17]J. F. Chang, H. H. Kuo, I. C. Leu, and M. H. Hon, Sens. Actuators B **84**, 258 (2002).
[18]M. Franke, T. Koplin, and U. Simon, Small **2**, 36 (2006).
[19]O. Kluth, G. Schöpe, B. Rech, R. Menner, M. Oertel, K. Orgassa, and H. Werner Schock, Thin Solid Films **502**, 311 (2006).

[20]F. K. Shan, G. X. Liu, W. J. Lee, and B. C. Shin, J. Appl. Phys. **101**, 053106 (2007).
[21]H. Zhu, H. Jia, D. Liu, Y. Feng, L. Zhang, B. Lai, T. He, Y. Ma, Y. Wang, J. Yin, Y. Huang, and Y. Mai, Appl. Surf. Sci. **258**, 6018 (2012).
[22]Y.-C. Cheng, Appl. Surf. Sci. **258**, 604 (2011).
[23]S. J. Kwon, Jpn. J. Appl. Phys. **44**, 1062 (2005).
[24]J. S. Jur and G. N. Parsons, ACS Appl. Mater. Interfaces **3**, 299 (2011).
[25]S. Kwon, S. Bang, S. Lee, S. Jeon, W. Jeong, H. Kim, S. C. Gong, H. J. Chang, H. Park, and H. Jeon, Semicond. Sci. Technol. **24**, 035015 (2009).
[26]H. B. Profijt, S. E. Potts, M. C. M. van de Sanden, and W. M. M. Kessels, J. Vac. Sci. Technol. A **29**, 050801 (2011).
[27]C. H. Ahn, H. Kim, and H. K. Cho, Thin Solid Films **519**, 747 (2010).
[28]V. Lujala, J. Skarp, M. Tammenmaa, and T. Suntola, Appl. Surf. Sci. **82–83**, 34 (1994).
[29]H. Saarenpää, T. Niemi, A. Tukiainen, H. Lemmetyinen, and N. Tkachenko, Sol. Energy Mater. Sol. Cells **94**, 1379 (2010).
[30]J. F. Moulder, W. F. Stickle, P. E. Sobol, and K. D. Bomben, *Handbook of X-Ray Photoelectron Spectroscopy: A Reference Book of Standard Spectra for Identification and Interpretation of XPS Data* (Physical Electronics Inc., Eden Prairie, 2005).
[31]E. Langereis, S. B. S. Heil, H. C. M. Knoops, W. Keuning, M. C. M. van de Sanden, and W. M. M. Kessels, J. Phys. D **42**, 073001 (2009).
[32]T. Tiwald, "*PSEMI*" *Oscillator Model* (Woollam Co. News, 2006), pp. 6–7.
[33]N. Ehrmann and R. Reineke-Koch, Thin Solid Films **519**, 1475 (2010).
[34]A. Pflug, V. Sittinger, F. Ruske, B. Szyszka, and G. Dittmar, Thin Solid Films **455–456**, 201 (2004).
[35]H. C. M. Knoops *et al.*, "Drude Modeling of Plasma-deposited ZnO: Electron Scattering at Different Length Scales," J. Appl. Phys. (to be published).
[36]S. Kasap and P. Capper, *Springer Handbook of Electronic and Photonic Materials*, 1st ed. (Springer, New York, 2006), pp. 30–31.
[37]S. K. Kim, C. S. Hwang, S.-H. K. Park, and S. J. Yun, Thin Solid Films **478**, 103 (2005).
[38]D. Kim, H. Kang, J.-M. Kim, and H. Kim, Appl. Surf. Sci. **257**, 3776 (2011).
[39]G. Luka, T. Krajewski, L. Wachnicki, B. Witkowski, E. Lusakowska, W. Paszkowicz, E. Guziewicz, and M. Godlewski, Phys. Status Solidi A **207**, 1568 (2010).
[40]A. Yamada, B. Sang, and M. Konagai, Appl. Surf. Sci. **112**, 216 (1997).
[41]J. W. Elam, D. Routkevitch, and S. M. George, J. Electrochem. Soc. **150**, G339 (2003).
[42]D.-J. Lee, H.-M. Kim, J.-Y. Kwon, H. Choi, S.-H. Kim, and K.-B. Kim, Adv. Funct. Mater. **21**, 448 (2011).
[43]J.-S. Na, G. Scarel, and G. N. Parsons, J. Phys. Chem. C **114**, 383 (2010).
[44]H. Tong, Z. Deng, Z. Liu, C. Huang, J. Huang, H. Lan, C. Wang, and Y. Cao, Appl. Surf. Sci. **257**, 4906 (2011).
[45]M. Gao, X. Wu, J. Liu, and W. Liu, Appl. Surf. Sci. **257**, 6919 (2011).
[46]X.-J. Yang, X.-Y. Miao, X.-L. Xu, C.-M. Xu, J. Xu, and H.-T. Liu, Opt. Mater. **27**, 1602 (2005).
[47]M. Chen, X. Wang, Y. H. Yu, Z. L. Pei, X. D. Bai, C. Sun, R. F. Huang, and L. S. Wen, Appl. Surf. Sci. **158**, 134 (2000).
[48]B.-Y. Oh, M.-C. Jeong, and J.-M. Myoung, Appl. Surf. Sci. **253**, 7157 (2007).
[49]R. W. Grant, J. R. Waldrop, S. P. Kowalczyk, and E. A. Kraut, J. Vac. Sci. Technol. **19**, 477 (1981).
[50]E. A. Kraut, R. W. Grant, J. R. Waldrop, and S. P. Kowalczyk, Phys. Rev. Lett. **44**, 1620 (1980).
[51]T. Nagata, O. Bierwagen, M. E. White, M. Y. Tsai, Y. Yamashita, H. Yoshikawa, N. Ohashi, K. Kobayashi, T. Chikyow, and J. S. Speck, Appl. Phys. Lett. **98**, 232107 (2011).
[52]J. Szuber, E. Bergignat, G. Hollinger, A. Polakowska, and P. Koscielniak, Vacuum **67**, 53 (2002).
[53]V. I. Nefedov, V. G. Yarzhemsky, A. V. Chuvaev, and E. M. Trishkina, J. Electron Spectrosc. Relat. Phenom. **46**, 381 (1988).
[54]J. Blomquist, J. Electron Spectrosc. Relat. Phenom. **36**, 69 (1985).
[55]L. Meda, C. Nicastro, F. Conte, and G. F. Cerofolini, Surf. Interface Anal. **29**, 851 (2000).
[56]T. Yamada, H. Makino, N. Yamamoto, and T. Yamamoto, J. Appl. Phys. **107**, 123534 (2010).
[57]K. Ellmer, A. Klein, and B. Rech, *Transparent Conductive Zinc Oxide* (Springer, New York, 2008).
[58]K. Ellmer and R. Mientus, Thin Solid Films **516**, 4620 (2008).
[59]J. Tauc, R. Grigorovici, and A. Vancu, Phys. Status Solidi B **15**, 627 (1966).
[60]H. Fujiwara and M. Kondo, Phys. Rev. B **71**, 075109 (2005).
[61]B. Elias, Phys. Rev. **93**, 632 (1954).
[62]G. Dingemans and W. M. M. Kessels, J. Vac. Sci. Technol. A **30**, 040802 (2012).